© 2020. Published by The Company of Biologists Ltd | Journal of Cell Science (2020) 133, jcs236471. doi:10.1242/jcs.236471

RESEARCH ARTICLE

SPECIAL ISSUE: CELL BIOLOGY OF THE IMMUNE SYSTEM

Reactive oxygen species-mediated cytoplasmic stiffening impairs the phagocytic ability of the macrophage

Mahesh Agarwal, Parijat Biswas, Anindita Bhattacharya and Deepak Kumar Sinha*

ABSTRACT

The phagocytic ability of macrophages empowers them to enforce innate immunity. RAW264.7, THP-1 and peripheral blood mononuclear cell-derived macrophages display considerable variability with regards to their phagocytic ability. We identify the underlying causes that attenuate the phagocytic abilities of a macrophage. Deformability of the cytoplasm and cortex influences the macrophage's phagocytic ability, and macrophages use the large cell-to-cell variability of their cytoplasmic stiffness to modulate their phagocytic ability. We find that the more-deformable macrophages have a higher phagocytic ability than those that are less deformable. Further, the subcellular spatial variability of cortex stiffness gives rise to more-deformable subdomains on the membrane for pathogen ingestion. We report a previously unknown negative-feedback loop that is triggered by the phagocytic oxidative burst. Macrophages utilize the excess reactive oxygen species to stiffen the cytoplasm, reducing their phagocytic propensity. In organisms, ageing or pathological conditions impair the phagocytic ability of macrophages. Our findings identify the targets that could potentially be utilized for restoring the phagocytic ability of the defunct macrophages.

KEY WORDS: Phagocytosis, ROS, Lamellipodial dynamics, Rheology

INTRODUCTION

Innate, as well as adaptive, immunity needs phagocytosis for the elimination of harmful microbes, apoptotic cells and their debris. Depending on the receptors involved in phagocytosis or the shape and size of the target particle, distinct molecular mechanisms facilitate the engulfment of the bacteria or particle. Regardless of the molecular machinery involved in phagocytosis, the mechanical deformability of a macrophage is expected to influence its phagocytic ability to engulf the bacteria or particle. The elastic (G') and viscous (G'') moduli are the parameters that define the deformability of a material. For a cell, the organization and dynamics of F-actin dictate its rheological properties (G' and G'') (Van Citters et al., 2006; Hale et al., 2009). Because of constant remodelling of the actin cytoskeleton, cells exhibit dynamic and frequency (ω)-dependent elastic [$G'(\omega)$] and viscous [$G''(\omega)$] moduli (Lee et al., 2010). $G'(\omega)$ and $G''(\omega)$ can be quantified by tracking the thermal fluctuations of the tracer particles embedded in the cytoplasm of the cells (passive microrheology) (Crocker and Hoffman, 2007; Tseng et al., 2002; Wirtz, 2009). Viscoelastic parameters are then obtained from the complex shear modulus:

$$G^*(\omega) = G'(\omega) + iG''(\omega) = \left\{\frac{2k_BT}{3\pi\alpha i\omega F_u[\Delta r^2(t)]}\right\},$$

where $F_u[\Delta r^2(t)]$ is the unilateral Fourier transform, k_BT is the thermal energy and α is the radius of the tracer particle (Mason et al., 1997; Wirtz, 2009). Although different cell types show characteristic values for $G^*(\omega)$, G' and G'' exhibit a log-normal distribution with large variance across the cells obtained from the same source and type (Papagiannopoulos et al., 2016). Wider distributions of G' and G'' imply that the deformability of the macrophages spans a wide range. It is unclear whether the wider range of cytoplasmic deformability of the macrophages gives rise to cells with distinct phagocytic ability. Because local actin turnover guides phagocytosis (Freeman and Grinstein, 2014), inhibition of actin polymerization reduces the F_c and C_3 receptor-mediated engulfment by macrophages (Kaplan, 1977). Thus, any cellular process that interferes with actin turnover is expected to influence the phagocytic ability of a macrophage. Phagocytosis of bacteria or the beads activates phagosome-associated NADPH oxidase (NOX) genes, causing localized production of reactive oxygen species (ROS) ($O_2^{\bullet-}$) within the phagosome (Dupré-crochet et al., 2013). $O_2^{\bullet-}$, being non-permeable, remains trapped in the phagosome to reach an estimated concentration of 1–4 M (Segal, 2005). However, because of the dismutation of $O_2^{\bullet-}$ into membrane-permeable H_2O_2, its concentration in the cytoplasm can be elevated to significant levels (Winterbourn et al., 2006). Cytoplasmic H_2O_2 can oxidize cysteine (thiol) residues of cytoplasmic proteins to attach the glutathione group to them with the help of glutathione *S*-transferase P (Grek et al., 2013). Glutathionylation of the Cys-374 residue of G-actin leads to about a 6-fold decrease in the rate of actin polymerization (Wang et al., 2001). Thus, we hypothesize that the H_2O_2 produced in response to engulfment of bacteria or particles by macrophages has the potential to reduce the rates of actin turnover because of glutathionylation (Sakai et al., 2013). This is then expected to alter the G' and G'' of the macrophages, and reduce the phagocytic ability of the macrophages that have already engulfed the bacteria or particle.

The phagocytic ability of a macrophage is known to be impaired by ageing and certain pathological conditions (Horn et al., 2014; Karavitis and Kovacs, 2011; Li et al., 2017; Liang et al., 2014; Carneiro et al., 2012; Mehta and Guidot, 2017; Taylor et al., 2005). Thus, it is important to understand the factors that can affect a macrophage's phagocytic ability. In this paper, we investigate whether the deformability (values of G' and G'') of the cytoplasm indeed affects the phagocytic ability of macrophages. The cortex of a cell is spatially heterogeneous, having softer and stiffer domains. Thus, we explore whether there are preferred sites on the membrane (having softer underlying cortex) for engulfment.

School of Biological Sciences, Indian Association for the Cultivation of Science, Jadavpur, Kolkata 32, India.

*Author for correspondence (bcdks@iacs.res.in)

M.A., 0000-0002-0529-0196; P.B., 0000-0003-2235-2384; D.K.S., 0000-0002-8303-5035

Received 12 July 2019; Accepted 17 January 2020

Journal of Cell Science (2020) 133, jcs236471. doi:10.1242/jcs.236471

RESULTS

A considerably large fraction of macrophages is incapable of phagocytosis

To explore the functional variability amongst the population of macrophages, we studied phagocytosis in differentiated RAW264.7 and THP-1 cells. To induce differentiation in these cells, we treated them with 50 ng/ml phorbol 12-myristate 13-acetate (PMA) for 2 days. As expected, differentiation caused cell cycle arrest in these cells (Fig. S1Ai,ii,B) (Han et al., 2013; Kosaka et al., 1996; Oliva et al., 2008). Although all the differentiated RAW264.7 (Fig. S1C) and THP-1 (Fig. S1D) cells express the macrophage marker CD68 (Bhattacharya et al., 2018), only a fraction of them could engulf bacteria (Fig. 1A) or beads (Fig. 1B; Movie 1). There could be two possible explanations for this: (1) insufficient supply or inadequate incubation time, which denied the macrophages the opportunity to engulf; or (2) the macrophages lacked the intrinsic ability of phagocytosis. To resolve the issue of opportunity as opposed to the ability to engulf, we enhanced the opportunity of phagocytosis by increasing the concentration of beads or bacteria (Fig. 1C) and the incubation time (Fig. 1D) for phagocytosis. Initially, the fraction of phagocytic macrophages increased with the concentration of bead and reached saturation at high concentrations. Despite the supply of a saturating number of beads or bacteria for a sufficient duration (Fig. 1D), a considerable fraction (more than 60%) of macrophages failed to engulf them. This, therefore, suggests the existence of macrophages intrinsically lacking phagocytic ability. Based on their phagocytic ability, we classified two distinct populations of macrophages: PH-Macrophage (capable of phagocytosis) and nPH-Macrophage (incapable of phagocytosis). All other phagocytosis experiments were performed in saturating conditions of bead concentration and incubation interval. We validated that the existence of the nPH-Macrophage population is not dependent on the nature of the object that the macrophages engulf (Fig. 1E,F), or the size of the microsphere (Fig. 1F), or the lineage of the macrophages, i.e. RAW267.4 and THP-1 cells (Fig. 1E) or peripheral blood mononuclear cells (PBMCs) (Fig. S1E).

To identify the root causes that gave rise to two distinct subpopulations of macrophages, we analysed various factors that may contribute to the phagocytic ability of a macrophage. First, we investigated whether the morphology of the macrophage influences its phagocytic ability. The size (spreading area) and circularity of macrophages exhibit significant heterogeneity, yet the propensity of phagocytosis is independent of the spreading area or circularity (Fig. S1F,G). This suggests that the observed variability (Fig. 1E; Fig. S1F,G) in a macrophage's ability to engulf does not arise from its morphological heterogeneity. Since the process of phagocytosis involves mechanical deformation of the cytoplasm, we hypothesized that cytoplasmic viscoelasticity can influence macrophages' phagocytic ability. Thus, heterogeneity in cytoplasmic viscoelasticity could give rise to the observed variability (Fig. 1E). Next, we investigated the link between the cytoplasmic viscoelasticity and phagocytic ability of macrophages.

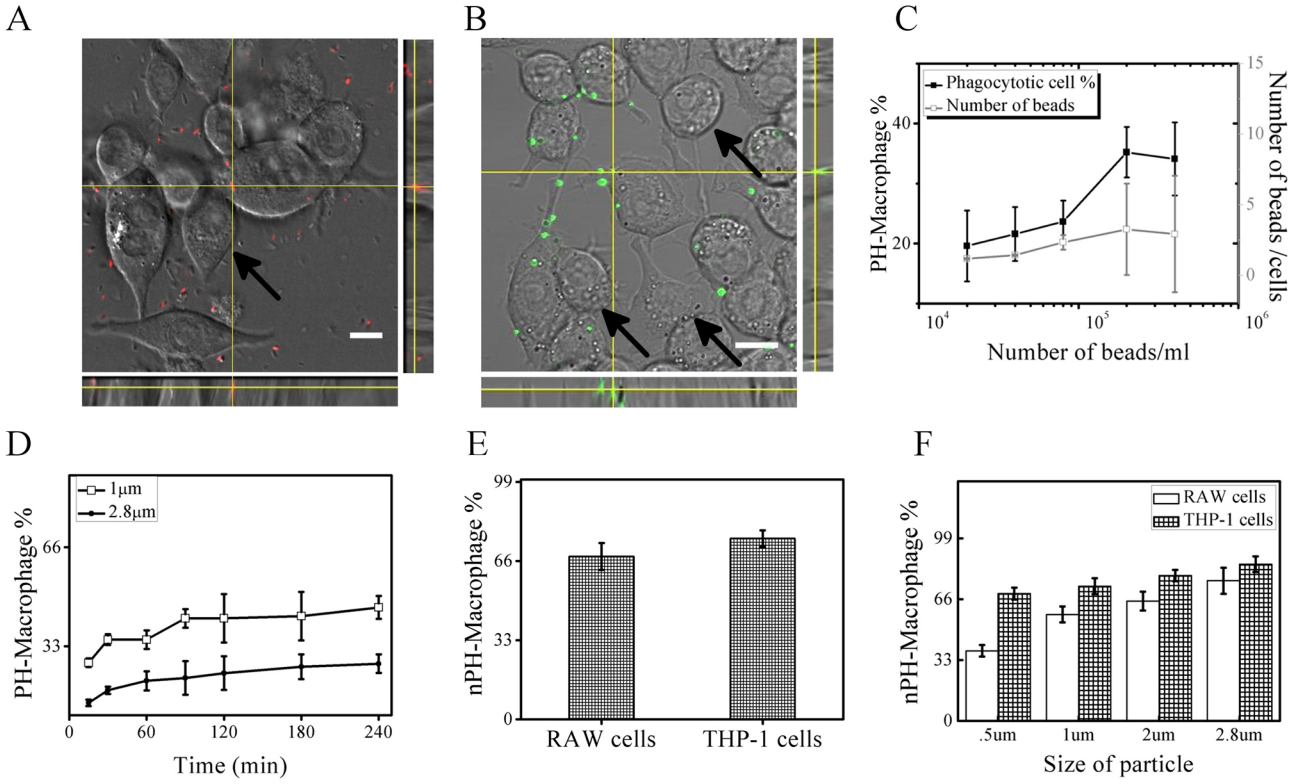

Fig. 1. A subpopulation of macrophages lacks phagocytic ability. (A,B) Overlaid DIC and fluorescence images of RAW264.7 cell-derived macrophage incubated with RFP-expressing bacteria (A, red) or 1 µm carboxylated fluorescence microspheres (B, green) for 2 h (arrows indicate cells lacking phagocytic ability, i.e. nPH-Macrophages). (C) Plot depicting the percentage of macrophages that engulf the beads (PH-Macrophages, black) and the average number of beads engulfed per cell by PH-Macrophages (grey) against the concentration of beads (radius 2.8 µm). (D) Plot depicting the percentage of macrophages that engulf the microsphere (radius 1 µm and 2.8 µm, supplied at saturating concentrations) against the incubation time. (E) Quantification of macrophages (derived from THP-1 and RAW264.7 cells) lacking phagocytic ability (nPH-Macrophages), incubated for 240 min at saturating concentrations of bacteria. (F) Quantification of macrophages lacking phagocytic ability (nPH-Macrophages) incubated for 240 min at saturating concentrations of particles (beads) of different sizes for phagocytosis. Scale bars: 10 µm. The error bars indicate the standard deviation from three or more independent experiments.

Journal of Cell Science (2020) 133, jcs236471. doi:10.1242/jcs.236471

Cytoplasmic stiffness influences the phagocytic ability of macrophages

Using single-particle-tracking microrheology (Chen et al., 2013; Hameed et al., 2012; Tseng et al., 2002), we studied the cytoplasmic viscoelasticity of fibroblast cells (NIH-3T3) (Fig. S2A–C). To establish the accuracy of our measurements of cytoplasmic viscoelasticity in the NIH-3T3 cells, we compared the reported values with our measurements. Our measured value of G' and G'' (43±15 Pa and 253±21 Pa.s, respectively; Fig. S2C at 10 Hz) are in good agreement with the values reported in the literature (Chen et al., 2013; Hameed et al., 2012; Tseng et al., 2002; Wirtz, 2009) Fig. 2A shows a differential interference contrast (DIC) image of a RAW264.7 cell-derived macrophage overlaid with the fluorescence image of the embedded tracer particles (200 nm polystyrene bead). We monitored the XY trajectories (Fig. 2A, inset) of five to ten beads/cells across 112 cells. The XY trajectories that exhibit drift

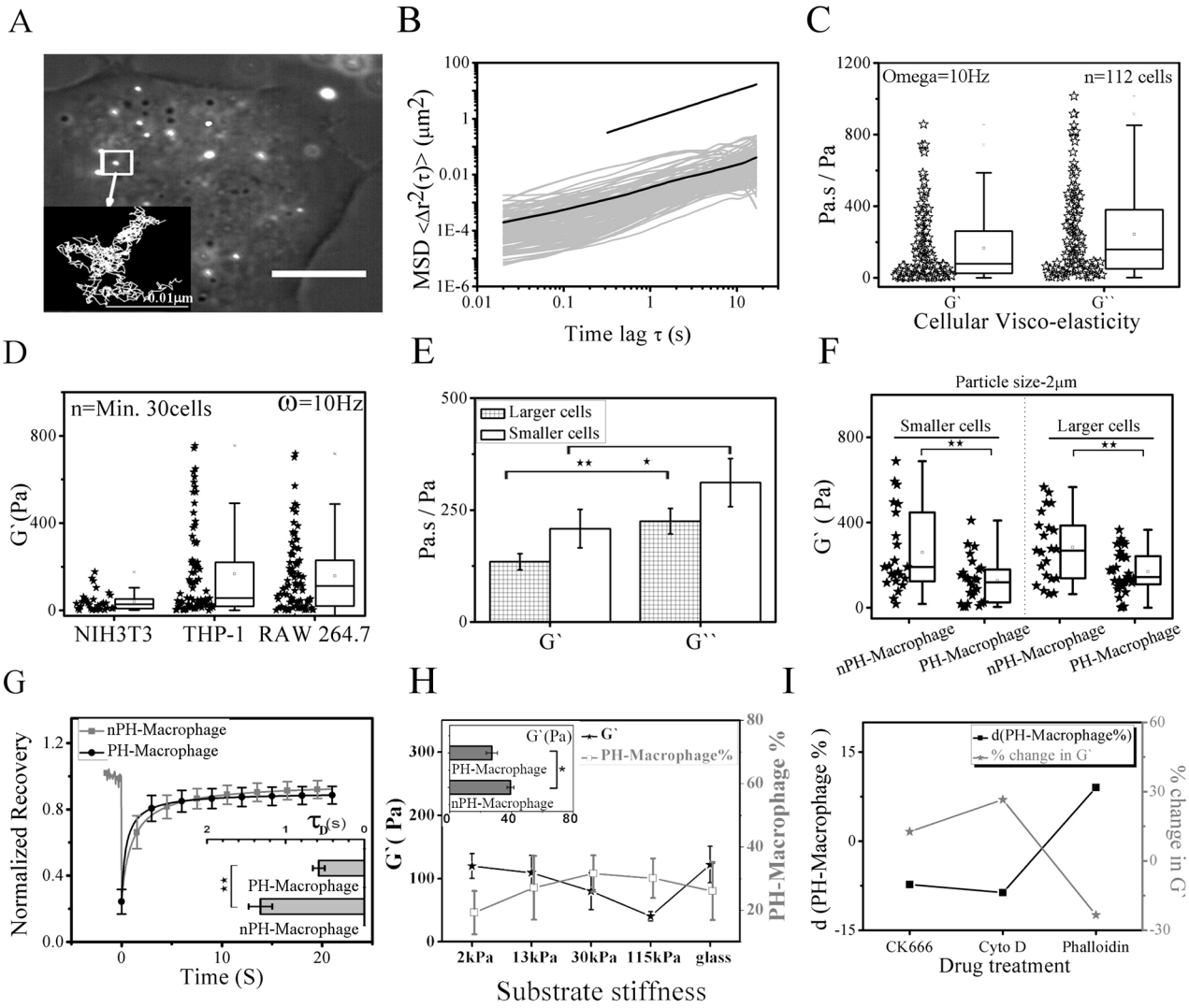

Fig. 2. PH-Macrophages have softer cytoplasm. (A) Overlaid DIC and fluorescence images (in greyscale) of 200 nm carboxylated polystyrene beads mechanically injected into RAW264.7 cells, which are simultaneously illuminated by low-intensity white light. A representative trajectory of a single bead is shown in the inset. (B) The mean square displacement (MSD, grey lines) and ensemble average of MSD (black lines) of beads embedded into the cytoplasm with respect to lag time (τ). (C) A box plot depicting the elastic moduli (G') and viscous moduli (G'') of RAW264.7 cells measured with 200 nm beads at ω=10 Hz (the measurement was performed on 112 cells). (D) Plot compares the cell-to-cell variability of cytoplasmic G' across different cell types. (E) Quantification of G' and G'' for smaller (spreading area <400 μm^2) and larger (spreading area >400 μm^2) RAW264.7 cells. Paired Student's *t*-tests were used to assess the significance of differences between the rheology of smaller and larger cells; *P<0.05, **P<0.01. (F) Comparison of cytoplasmic stiffness (G') of PH-Macrophages with that of nPH-Macrophages; 2 μm beads are used for phagocytosis. Paired Student's *t*-tests were used to assess the significance of differences between the rheology of PH-Macrophages and nPH-Macrophages; **P<0.01. (G) Normalized fluorescence recovery of actin–GFP after photobleaching PH-Macrophages and nPH-Macrophages. A comparison of the characteristic recovery timescale (τ_D, in s) fitted to a single exponential recovery model for actin–GFP in PH-Macrophages with that of nPH-Macrophages is shown in the inset. Paired Student's *t*-tests were used to assess the significance of differences between recovery timescales (τ_D, in s) of aPR-Macrophages and iPR-Macrophages; **P<0.01. (H) Comparison of the percentage of PH-Macrophages with the corresponding cytoplasmic G' when the cells are cultured on substrates of different stiffness. Phagocytosis was assayed using 2 μm beads. A comparison of the G' of PH-Macrophages and nPH-Macrophages cultured on a 115 kPa substrate is shown in the inset. Paired Student's *t*-tests were used to assess the significance of differences between the rheology of PH-Macrophages and nPH-Macrophages; *P<0.05. (I) Comparison of the percentage changes in PH-Macrophages with the percentage change in cytoplasmic G' when the cells are treated with CK666 (50 μM), Cytochalasin D (2 μM) and phalloidin oleate (10 μM). Boxes represent the 25–75th percentiles, and the median is indicated. The whiskers show the complete range from minimum to maximum values. Points on the left side of graphs show all values. Scale bar: 10 μm. The error bars indicate the standard deviation from three or more independent experiments.

Journal of Cell Science

Journal of Cell Science (2020) 133, jcs236471. doi:10.1242/jcs.236471

(caused by the mechanical shift of the stage or cell migration) were excluded from our analysis for estimation of G' and G''. Particle-tracking microrheology provides the local value of viscoelasticity; therefore, in all experiments we selected beads in the mid-plane (2 µm above the basal plane) for G', G'' calculations. Fig. 2B depicts the mean square displacement (MSD) of all the legitimate tracer particles from which the G' and G'' values are computed. For RAW264.7 macrophages, the average values of G' and G'' are 153±17.83 Pa and 205±17.68 Pa.s, respectively (Fig. 2C), whereas for THP-1 cell-derived macrophages the average values of G' and G'' are 179±21 Pa and 259±27 Pa.s, respectively (Fig. S2D–F). This suggests that the macrophages (i.e. differentiated RAW264.7 and THP-1 cells) have stiffer cytoplasm compared to that of the fibroblasts (Fig. S2G). The rheological parameters (G' and G'') of macrophages exhibit higher cell-to-cell variability compared to those of fibroblast cells (Fig. 2D). The cytoplasmic G' and G'' of a cell are determined primarily by the dynamics of the intracellular network of the filaments such as actin (Flores et al., 2019; Gardel et al., 2008; Mofrad, 2009) and intermediate filaments (Block et al., 2015). As a result, we observe that cellular spreading is inversely correlated with the cytoplasmic G' and G'' of the macrophage (Fig. S2H). To study the effect of G' and G'' on the phagocytic ability of a macrophage, we classified the macrophages into two subgroups based on their spreading area. This was done to mitigate the heterogeneity in G', G'' that arises from its dependence on spreading area (Fig. S2H). We set the median size (Fig. S2I) as the cut-off for classifying the macrophages into large and small subgroups. Fig. 2E shows the G' and G'' of the smaller and larger macrophages, suggesting that the cytoplasm of the macrophage becomes 'softer' and 'less viscous' upon spreading. Lowering of viscous modulus (G'') due to spreading (Fig. S2H) was independently validated by measuring the diffusion coefficient of monomeric EGFP using fluorescence recovery after photobleaching (FRAP) (Fig. S2K). To study the relationship between the cytoplasmic viscoelasticity (G', G'') and the phagocytic ability of the macrophages, we compared the G' (Fig. 2F) and G'' (Fig. S2L) of PH-Macrophages and nPH-Macrophages in differentiated RAW-264.7 (Fig. S3A–F) and THP-1 (Fig. S3G–L) cells with beads of different sizes (Fig. S3) and RFP-expressing bacteria (Fig. S2M,N). Irrespective of the size of the phagocytic bead or the nature of particle engulfed (beads or bacteria), PH-Macrophages have softer and less viscous cytoplasm (Fig. S3) compared to nPH-Macrophages in RAW264.7 and THP-1 cell lines. Softer cytoplasm of PH-macrophages indicates lower cross-linking or higher rates of turnover of actin subunits, resulting in a higher fraction of monomeric actin. We independently confirmed the higher rates of actin turnover in PH-macrophages using FRAP. As shown in Fig. 2G, we observed two times faster recovery rates of actin–GFP in PH-Macrophages compared to that in nPH-Macrophages, reconfirming the higher actin turnover in PH-Macrophages. Similar high rates of actin turnover were observed in PH-Macrophages and nPH-Macrophages when challenged with bacteria (Fig. S2Jii). To establish the link between the cytoplasmic viscoelasticity and the phagocytic ability of macrophages, we altered the G' of the macrophages. Cytoplasmic rheology was altered in two independent experiments to further confirm its influence on phagocytic ability (Fig. 2H,I). The stiffness of the substrate that cells adhere to influences its cytoplasmic rheology (Gupta et al., 2015; Yeung et al., 2005). Fig. 2H depicts the cytoplasmic G' of macrophages cultured on substrates of varying stiffness. As expected, the propensity of phagocytosis (% PH-Macrophage) exhibits an inverse dependence on cytoplasmic G' (Fig. 2H) (i.e. an increase in G' leads to a decrease in phagocytosis and vice versa). The inset in Fig. 2H suggests that the PH-Macrophages have softer cytoplasm than the nPH-Macrophages on 115 kPa substrate (having the softest cytoplasm as well). The actin cytoskeleton is one of the key components that dictate cytoplasmic rheology. We targeted the actin cytoskeleton with drugs such as Cytochalasin D, CK666 and phalloidin oleate, to alter the G' of the macrophages. Although these drugs do have other unintended effects on cells, we observe that the propensity of phagocytosis (in drug-treated macrophages) exhibits an inverse dependence on cytoplasmic G'. Thus, we hypothesize that softer cytoplasm in a macrophage increases the propensity of phagocytosis.

Softer cytoplasm indicates faster actin turnover (Wirtz, 2009). The rate of turnover of actin subunits in the lamellipodia is higher than that in other regions of cells (Ponti et al., 2005; Theriot and Mitchison, 1991). As a result, we expect that the macrophages with lamellipodia would have softer cytoplasm and would exhibit higher phagocytic propensity than macrophages that lack lamellipodia.

Macrophages lacking protrusion-retraction activity are incapable of phagocytosis

The lamellipodial regions of a cell often exhibit protrusion-retraction activity (Fig. 3A; Movie 2). The macrophages that lack lamellipodia exhibit significantly lesser protrusion-retraction activity. Using protrusion-retraction activity, we classified the macrophages into active (has protrusion-retraction activity) and inactive (lacks protrusion-retraction activity) groups as described below. To visualize the macrophages that have the regions undergoing protrusion-retraction activity, we acquired time-lapse images, then calculated the standard deviation (s.d.) on all pixels along the time axis (Fig. 3A, right; Movies 2 and 3). The peripheral regions of the cells with higher protrusion-retraction activity (aPR, active protrusion-retraction) appear as diffused red-yellow colour (indicated by the single-headed arrow in Fig. 3A, right), whereas the regions lacking protrusion-retraction activity (iPR, inactive protrusion-retraction) appear as a sharply defined boundary (mostly in blue and indicated by the double-headed arrow in Fig. 3A, right). Macrophages that lack aPR regions are classified as iPR-Macrophages, whereas cells possessing even a single aPR domain are classified as aPR-Macrophages. As expected, cells in the aPR-Macrophage group possess softer cytoplasm compared to cells in the iPR-Macrophage group (Fig. 3B). The softer cytoplasm further manifests in enhanced phagocytic ability, while none of the macrophages in the iPR-Macrophage group possess any phagocytic ability (Fig. S4A,B). Only 36% of aPR-Macrophages exhibit phagocytic ability for beads 2.8 µm in size (Fig. 3C). This suggests that protrusion-retraction activity is necessary but not sufficient for the engulfment of microspheres, beads or bacteria (Fig. S4A,B) by aPR-Macrophages. To further investigate the role of protrusion-retraction activity in phagocytosis, we analysed the time lapse of the bead engulfment process by aPR-Macrophages for 1 h. Fig. 3D depicts three different possible cases (A, B and C) in the time period of the bead-engulfment process through the aPR region: Case A, when the beads approach and retreat after a brief interaction with an aPR region; Case B, when the beads approach and stick to the aPR region, yet the macrophage fails to engulf them during the 1 h incubation; and Case C, when the beads are engulfed through the aPR region. Even in the aPR-Macrophage group, no bead or bacteria is ever engulfed through the iPR region of the cell. Fig. 3E quantifies the percentage of observed events in cases A, B and C in aPR-Macrophages. Although the propensity of engulfment through iPR regions remain zero for all sizes of beads, the propensity of

Journal of Cell Science (2020) 133, jcs236471. doi:10.1242/jcs.236471

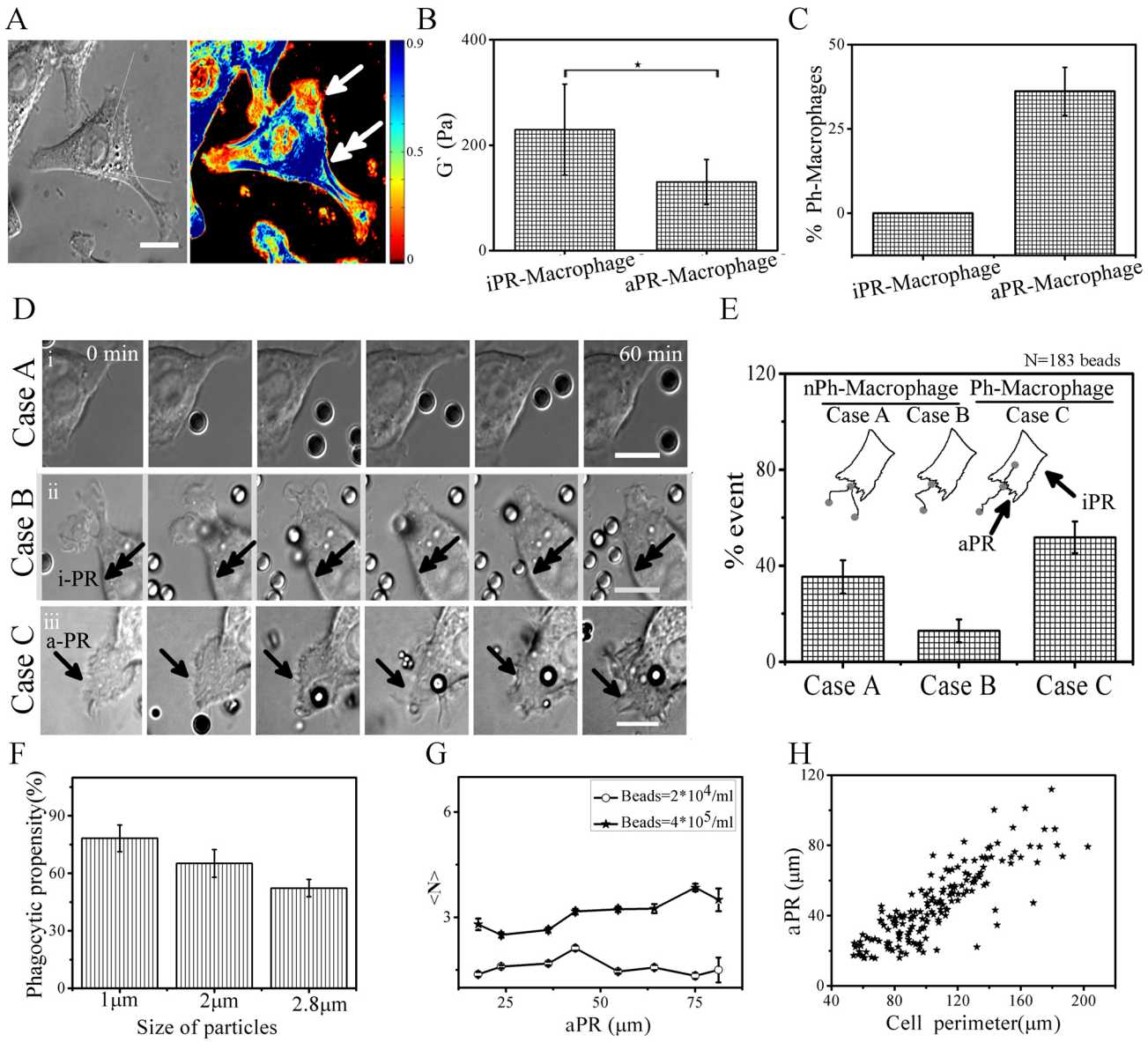

Fig. 3. Specific domains on the macrophage membrane engulf bead. (A) Representative DIC (left) and normalized s.d. (right) images obtained from the DIC time lapse. Colour bar depicts the normalized s.d. values. The single-headed arrow points to the region of higher protrusion-retraction activity (aPR), whereas the double-headed arrow points to the regions that lack (inactive) protrusion-retraction activity (iPR). (B) Comparison of the cytoplasmic elastic moduli values of the aPR-Macrophages and iPR-Macrophages. Paired Student's *t*-tests were used to assess the significance of differences between the rheology of aPR-Macrophages and iPR-Macrophages; **P*<0.05. (C) Plot depicting the percentage of PH-Macrophages amongst the aPR-Macrophage and iPR-Macrophage categories. (D) DIC time-lapse images of RAW264.7 macrophages incubated with beads (2.8 µm) for phagocytosis. (i) The condition (Case A) when a microsphere comes into contact with a macrophage, but the macrophage fails to capture it. (ii) The condition (Case B) when a microsphere is captured by a macrophage yet it fails to engulf the microsphere. (iii) The condition (Case C) when the macrophage successfully engulfs the microsphere. (E) Quantification of Case A, Case B and Case C out of 183 observed events (microsphere-macrophage interaction). A schematic of Case A, Case B and Case C along with microsphere trajectories is shown above the chart. (F) The propensity of phagocytosis through aPR regions in PH-Macrophages. (G) The correlation between the perimeter of a PH-Macrophage and the abundance of aPR regions. aPR is quantified by its total contour length along the perimeter. (H) The average number of beads engulfed by PH-Macrophages *n* against the abundance of aPR regions when macrophages are challenged with different concentrations of particles. Scale bars: 10 µm. The error bars indicate the standard deviation from three or more independent experiments.

engulfment through aPR regions depends on the size (Fig. 3F) or the nature (Fig. S4C) of the object being engulfed. Only 52%, 79%, 57% and 46% of macrophages in aPR-Macrophage group possess the phagocytic ability for bacteria, and 0.5 µm, 1 µm and 2 µm particles, respectively (Fig. S4C).

Our findings suggest that the PH-Macrophages with more aPR regions must engulf more beads compared to PH-Macrophages with fewer aPR regions. Thus, the extent of phagocytosis, N (number of beads engulfed by the macrophage), is expected to be proportional to the abundance of the aPR regions [i.e. $\langle N\rangle = C\times X\times Pe\times p$, where C is the collision frequency of the bead with the aPR region of the macrophage, Pe is the perimeter of the cell, X is the fraction of the aPR regions and p is the probability of engulfment]. Here, C is a tunable parameter (dependent on bead concentration), and X and Pe are measurable quantities. As expected, the reduction of C at a given value of $X\times Pe$ (abundance of aPR regions) lowers the N (Fig. 3G).

Journal of Cell Science (2020) 133, jcs236471. doi:10.1242/jcs.236471

Macrophages with longer perimeters have more aPR regions (Fig. 3H). Therefore, bigger macrophages are expected to engulf more beads. However, contrary to our expectations, we observed that the extent of phagocytosis [i.e. $\langle N \rangle$] is independent of the abundance of aPR regions ($X \times Pe$) in the PH-Macrophages (Fig. 3G). This suggests that, in a PH-Macrophage, there is a possibility of a negative-feedback loop that is triggered because of the engulfment of the beads, which inhibits further phagocytosis events.

Phagocytosis by PH-Macrophages reduces their ability for further phagocytosis

Next, we investigated whether phagocytosis by PH-Macrophages indeed reduces their phagocytic ability. For this, we performed a dual phagocytosis assay with the same sized beads (Fig. 4A) or the bacteria (Fig. S4D) of different colours (fluorescence emission). The differentiated RAW264.7 cells were first supplied with green fluorescent beads or bacteria for phagocytosis, then the same cells

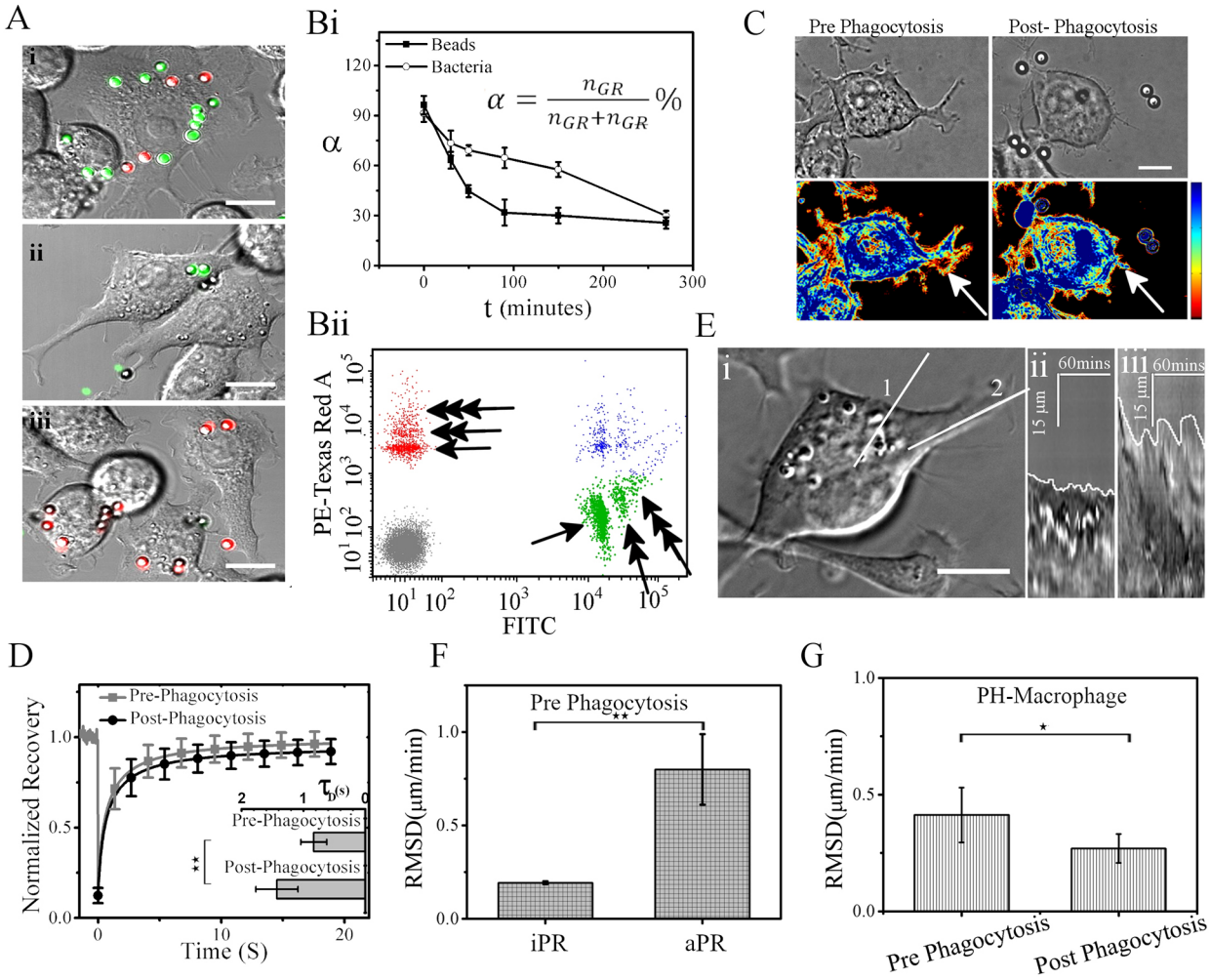

Fig. 4. Macrophages lose their phagocytic ability after phagocytosis. (A) Fluorescence images of 2 µm fluorescent carboxylated beads superimposed on DIC images of RAW264.7 cell-derived macrophages. (i) Representative images of PH-Macrophages that engulfed both the green and red beads in the dual-bead phagocytosis assay. (ii) A representative image of a PH-Macrophage that engulfed the green and not the red beads in the dual-bead phagocytosis assay. (iii) A representative image of a PH-Macrophage that failed to engulf the green beads but did engulf the red beads in the dual-bead phagocytosis assay. (B) (i) Plot depicting the percentage of PH-Macrophages that retain their phagocytic ability (α) until time 't' for phagocytosis of 2 µm beads (filled circles) and bacteria (open circles). n_{GR} is the number of PH-Macrophages that have engulfed both green and red particles (beads or bacteria), n_G is the number of PH-Macrophages that have engulfed only the green particles but not the red particles. (ii) FACS scatter plot of macrophages after the dual-bead phagocytosis assay. Grey, green, red and blue are macrophages that have engulfed no, only green, only red or both the beads, respectively, after the dual-bead phagocytosis assay. One, two or three heads in the arrow indicate the number of beads engulfed by the macrophages. FITC, fluorescein isothiocyanate. (C) Normalized s.d. images (lower row) obtained from corresponding DIC time-lapse images (upper row) indicates loss of protrusion-retraction activity after engulfment (region indicated by the arrows). (D) Normalized fluorescence recovery after photobleaching (FRAP) of actin–GFP in pre-phagocytic and post-phagocytic states of the same macrophage. Quantification of the characteristic recovery timescale (τ_D, in s) fitted to a single exponential recovery model for actin–GFP from 17 cells is shown in the inset. Paired Student's t-tests were used to assess the significance of differences between the recovery timescale (τ_D, in s) of aPR-Macrophages and iPR-Macrophages; $^{**}P<0.01$. (E) (i) DIC image of a RAW264.7 cell macrophage. The white lines 1 and 2 show the iPR and aPR region, respectively. The kymographs for 60 min duration along line 1 in the iPR region and along line 2 in the aPR region are shown in Eii and Eiii, respectively. (F) Plot depicting the root mean square displacement (RMSD) of the edge of the cell (white curve) as observed in the kymographs in Eii and Eiii. Paired Student's t-tests were used to assess the significance of differences between RMSD of the aPR and iPR regions; $^{**}P<0.01$. (G) RMSD of the edge of the cell averaged over many kymographs in the aPR regions of a PH-Macrophage, before and after particle engulfment. Paired Student's t-tests were used to assess the significance of differences between RMSD of pre-phagocytosis and post-phagocytosis; $^{*}P<0.05$. Scale bars: 10 µm. The error bars indicate the standard deviation from three or more independent experiments.

Journal of Cell Science (2020) 133, jcs236471. doi:10.1242/jcs.236471

were supplied with red fluorescent beads or bacteria after a waiting period 't' for the second round of phagocytosis (Fig. 4A,B; Fig. S4D). In dual phagocytosis assay, we observed four distinct cases. Class 1 macrophages are macrophages that have engulfed both the green and the red beads. These macrophages have been able to maintain their phagocytic ability until the second phagocytosis assay (Fig. 4Ai), i.e. they have remained PH-Macrophages during the period of the assay, 't'. Class 2 macrophages are macrophages that have engulfed the green beads during the first phagocytosis assay but failed to engulf the red beads during the second phagocytosis assay. These macrophages have not been able to maintain their phagocytic ability until the second phagocytosis assay (Fig. 4Aii), i.e. they have switched from PH-Macrophage to nPH-Macrophage during the period of the assay, 't'. Class 3 macrophages are macrophages that did not engulf the green beads but engulfed the red beads. These macrophages have gained phagocytic ability (Fig. 4Aiii), i.e. they have switched from nPH-Macrophage to PH-Macrophage during the period of the assay, 't'. Class 4 macrophages are macrophages that did not engulf either type of bead during the phagocytosis assay. These macrophages have remained as nPH-Macrophages throughout the assay. Using the dual-bead phagocytosis assay, we estimated the percentage of PH-Macrophages (α) that are able to retain their phagocytic ability throughout duration 't' after the first the first round of phagocytosis: $\alpha = \frac{n_{GR}}{n_{GR}+n_G}\%$, where n_{GR} is the number of PH-Macrophages that have engulfed both the green and red beads or bacteria, whereas n_G is the number of PH-Macrophages that have engulfed only the green beads or bacteria and not the red beads or bacteria. Using fluorescence images of a minimum of 20 randomly chosen fields of view, we counted n_{GR} and n_G to evaluate α. Fig. 4B depicts the gradual loss of phagocytic ability of a PH-Macrophage after phagocytosis of beads or bacteria. To increase the statistics of n_{GR} and n_G, we repeated the dual-bead phagocytosis experiment and counted the cells with fluorescence-activated cell sorting (FACS) (Fig. 4Bii). Using larger statistics of cells, we re-verified the gradual loss of phagocytic ability of the PH-Macrophages after engulfment of the bead or bacteria (Fig. S4E). The loss of the phagocytic ability of a PH-Macrophage is concurrent with the loss of its protrusion-retraction activity (Fig. 4C; Movies 4 and 5) and the actin turnover rates (Fig. 4D). Fig. 4C shows a representative image of an aPR-Macrophage that loses its protrusion-retraction activity after engulfment. As expected (from Fig. 2G), loss of phagocytic ability increases the recovery time of actin–GFP as per the FRAP experiments (Fig. 4D). The same phenomenon was verified with the bacterial phagocytosis assay (Fig. S4F). We quantified the protrusion-retraction activity to study the effect of bead engulfment on the protrusion-retraction activity of a PH-Macrophage. For this, we computed kymographs in iPR (along line 1 in Fig. 4Ei) and aPR (along line 2 in Fig. 4Eiii) regions of the macrophages. Fig. 4E depicts the respective kymographs along lines 1 (Fig. 4Eii) and 2 (Fig. 4Eiii) in Fig. 4Ei. We computed the root mean square displacement (RMSD) of the cell edge (along the white line indicated in Fig. 4Eii,iii) to quantify the protrusion-retraction activity. Fig. 4F compares the average protrusion-retraction activity in iPR and aPR regions of an aPR-Macrophage (before it has engulfed the particle). As expected, iPR regions of the aPR-Macrophage exhibit lower RMSD than do the aPR regions. Fig. 4G depicts the reduction in RMSD in the aPR region of PH-Macrophages post-phagocytosis. Thus, using a dual-bead phagocytosis assay, we established that the phagocytic ability of a PH-Macrophage monotonically decreases after engulfment of a bead. Therefore, we hypothesize that the engulfment of the bead by PH-Macrophages triggers a negative-feedback loop that inhibits its ability for further phagocytosis.

ROS generated by bead engulfment reduce the phagocytic ability of a PH-Macrophage

Next, we investigated the mechanism by which engulfment of a bead causes inhibition of further phagocytosis. Since higher rates of actin turnover are associated with a higher phagocytic ability (Figs 4D and 2G), we considered various phagocytosis-mediated biochemical alterations within the PH-Macrophages that have the potential to reduce actin turnover. Within a few minutes of bead engulfment, the elevated levels of ROS ($O_2^{\bullet -}$) (Dupré-crochet et al., 2013) in PH-Macrophages have the potential to reduce the rates of actin turnover by glutathionylation (Sakai et al., 2013; Stojkov et al., 2017). Therefore, we hypothesize that the ROS generated due to bead or bacteria engulfment decrease the rates of actin turnover, hence reducing the phagocytic ability of the PH-Macrophages. To validate this hypothesis, we compared the ROS levels in PH-Macrophages with those in the nPH-Macrophages (Fig. 5A,B). PH-Macrophages possess significantly higher levels of ROS compared to nPH-Macrophages (Fig. 5A; Fig. S5A), which was again validated by FACS (Fig. 5B,C). Using FACS analysis, we were able to generate large statistics on the level of 2′,7′-dichlorodihydrofluorescein diacetate (H_2DCFDA) fluorescence and the number of engulfed beads (Fig. S5B). We observed a positive correlation between the level of ROS (H_2DCFDA fluorescence) and the number of beads engulfed by the PH-Macrophages (Fig. 5D). To establish that the intracellular ROS could adversely affect a macrophage's phagocytic ability, we analysed the fold change in percentage of PH-Macrophages in response to directly perturbed ROS levels. Differentiated RAW264.7 cells were treated with 250 µM H_2O_2 or 500 µM vitamin C for 1 h to alter the intracellular ROS levels. Fig. 5E establishes that treatment with H_2O_2 increases the ROS levels (as measured by H_2DCFDA fluorescence) and decreases the fraction of PH-Macrophages. The protrusion-retraction activity of the H_2O_2-treated cells is also attenuated (Movies 6 and 7). Further decreasing the ROS levels by the antioxidant vitamin C increases the fraction of PH-Macrophages (Fig. 5E). The inverse dependence of phagocytic ability on the ROS levels establishes that ROS adversely affect the phagocytic ability of differentiated RAW264.7 cells. We further demonstrate that ROS affect actin turnover to alter the phagocytic ability of RAW264.7 cells. Fig. 5F establishes that an increase in ROS levels decreases the protrusion-retraction activity (RMSD) and increases the actin–GFP recovery timescale (τ_D) of actin–GFP, as well as the cytoplasmic stiffness (Fig. S5C, G' inset, G''), whereas a decrease in ROS increases the protrusion-retraction activity (RMSD), and reduces the τ_D of the actin–GFP in RAW264.7 cells as well as the cytoplasmic stiffness. Thus, a higher cellular ROS level reduces actin turnover, which decreases the protrusion-retraction activity and, in turn, adversely affects macrophages' phagocytic ability. If the ROS generated by the bead engulfment are responsible for the loss of phagocytic ability, then treatment with vitamin C must rescue this loss. Fig. 5G demonstrates that treatment with vitamin C does indeed rescue the loss of phagocytic ability during the dual-bead phagocytosis assay in PH-Macrophages. Glutathionylation of the Cys-374 residue of G-actin is known to decrease the rate of actin polymerization (Wang et al., 2001). Fig. 5H compares the levels of glutathionylation of actin among control macrophages (not challenged with pathogen), nPH-Macrophages and PH-Macrophages, in the presence or absence of

Journal of Cell Science (2020) 133, jcs236471. doi:10.1242/jcs.236471

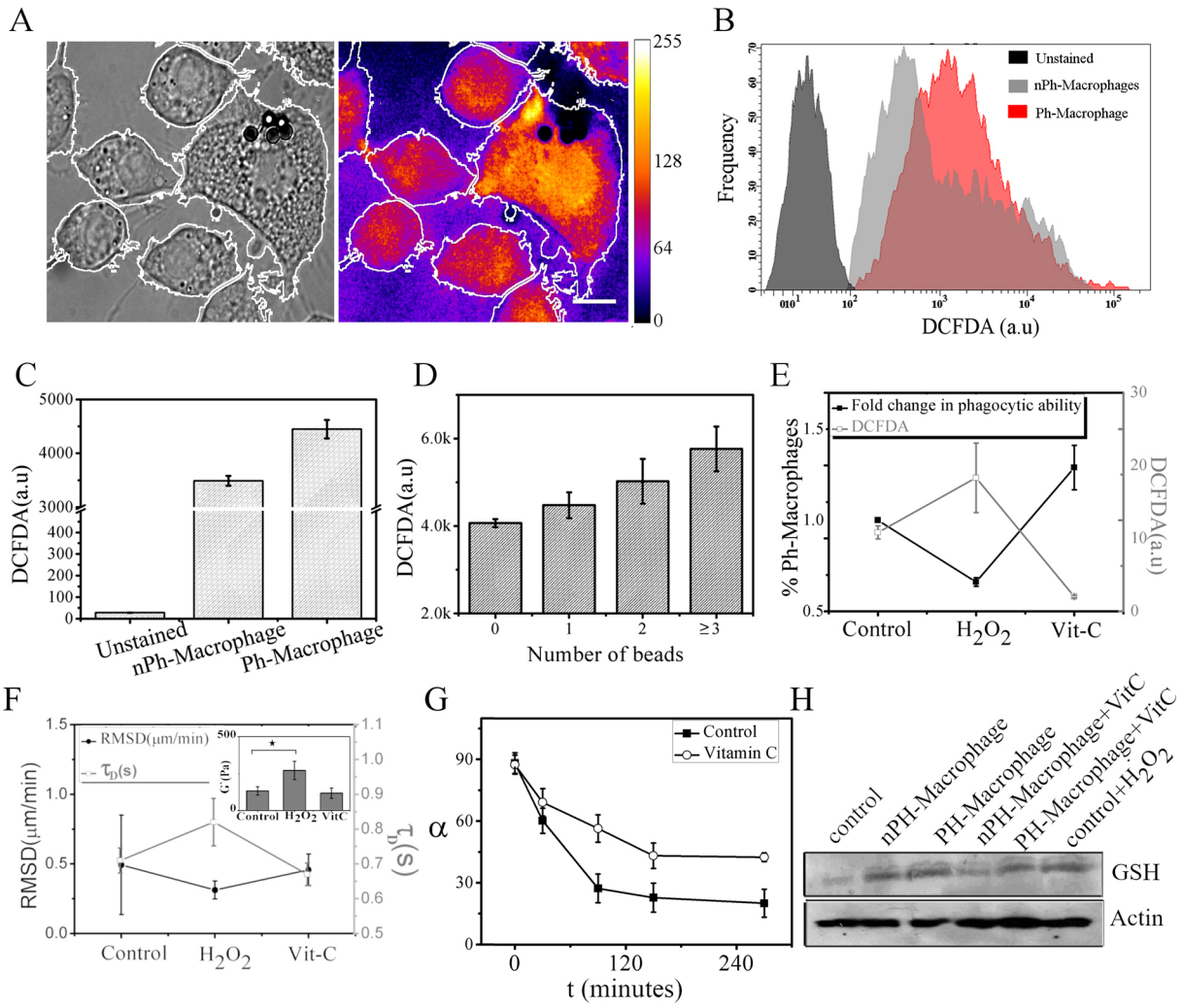

Fig. 5. ROS reduces the phagocytic ability of a PH-Macrophages. (A) DIC (left) and fluorescence (right) image of H_2DCFDA-treated RAW264.7 cell-derived macrophage after phagocytosis assay with beads (2.8 µm). The colour bar (Fire LUT, ImageJ) depicts the H_2DCFDA fluorescence levels. (B) Histograms obtained from FACS, depicting H_2DCFDA fluorescence levels in PH-Macrophages, nPH-Macrophages and macrophages not treated with H_2DCFDA (unstained). (C) Mean H_2DCFDA fluorescence levels in PH-Macrophages, nPH-Macrophage and macrophages not treated with H_2DCFDA (unstained). (D) Average H_2DCFDA fluorescence levels in macrophages that have engulfed 0, 1, 2 and ≥3 beads. (E) Fold change in percentage of PH-Macrophages when the cells are treated with H_2O_2 (250 µM) or vitamin C (500 µM) for 1 h before the phagocytosis assay; corresponding levels of H_2DCFDA fluorescence are indicated in grey. (F) The change in RMSD (black) in the aPR region and in the recovery timescale (grey) of actin–GFP in RAW264.7 cell-derived macrophages when the cells are treated with H_2O_2 or vitamin C. The change in cytoplasmic G' under the same treatment protocol is shown in the inset; *P<0.05. (G) Loss of phagocytic ability (α) of PH-Macrophages in control and vitamin C-treated cells. (H) Immunoblot of glutathionylated-actin (anti-GSH) after immunoprecipitation with anti-β-actin. Scale bar: 10 µm. The error bars indicate the standard deviation from three or more independent experiments.

vitamin C (500 µM), a well-established ROS scavenger. Unchallenged cells treated with 250 µM H_2O_2 served as a positive control. The immunoblot (Fig. 5H) shows that cells treated with vitamin C during the phagocytosis assay exhibit less actin glutathionylation than untreated cells. Quantification of the blot is shown in Fig. S5C. This establishes that the elevated levels of ROS in PH-Macrophages glutathionylate actin, and establishes that the ROS generated by bead or bacteria engulfment affect the rates of actin turnover to reduce the phagocytic potential of a PH-Macrophage.

DISCUSSION

Macrophages are a physiologically heterogeneous group of cells (Gordon and Taylor, 2005; Jain et al., 2019; Segal, 2005; Varol et al., 2015) and perform distinct immunological functions (Horn et al., 2014; Lavin et al., 2014). Literature suggests that the phagocytic ability of macrophages is impaired because of ageing (Horn et al., 2014) and pathogenic conditions such as HIV infection (Taylor et al., 2005) or chronic alcohol ingestion (Mehta and Guidot, 2017). In certain conditions, the loss of phagocytic ability is ascribed to the reduction of receptors (Mehta and Guidot, 2017); in other conditions, it is the impaired actin turnover that incapacitates macrophages of their phagocytic ability (Li et al., 2017). Cytoplasmic deformability impacts multiple physiological processes, such as cell morphology, proliferation, migration and differentiation. Further crucial cellular functions, such as the ability to migrate through a 3D porous microenvironment, are influenced by the cytoplasmic deformability. Engulfment during phagocytosis involves considerable deformation of the cortex and the cytoplasm of the cell. Therefore, we hypothesized that the mechanical deformability (compliance) of a macrophage cytoplasm must be one of the critical biophysical parameters that influence its

Journal of Cell Science (2020) 133, jcs236471. doi:10.1242/jcs.236471

phagocytic ability. The tracer particles in the mid-plane (2 µm above the basal plane) were chosen to estimate the cytoplasmic G' and G'' of the macrophages. This was done to mitigate the effect of heterogeneous cytoplasmic rheology at subcellular scales. The mechanical deformability of cortex and the cytoplasm depends on its complex shear modulus ($G^*=G'+iG''$). Hence, G^* is expected to influence the ability of the macrophages to engulf pathogens. Therefore, a systematic investigation is required to understand the impact of cytoplasmic deformability on the phagocytic ability of the macrophage. G^* exhibits a broad distribution, i.e. larger cell-to-cell variability (Fig. 2D) compared to other cells. This paper establishes that the macrophages utilize the larger cell-to-cell variability of G^* to modulate their phagocytic ability. Macrophages with more deformable (softer, lower G') cytoplasm have higher phagocytic ability. Further, the subcellular spatial variability of G^* causes preferred subdomains on the membrane for the ingestion of a pathogen. Macrophages ingest pathogens exclusively through specific micro-domains with higher deformability (aPR regions) of the underlying cortex. Although phagocytosis happens exclusively through the aPR regions, the macrophages with larger aPR regions do not seem to ingest more pathogens. This led us to discover a negative-feedback loop that is triggered by the intracellular ROS generated in response to ingestion of beads or bacteria. ROS cause actin glutathionylation, which adversely affects the actin turnover rates. This leads to stiffening of the cortex and the cytoplasm and incapacitation of the macrophage's ability for further ingestion (Fig. 6). However, in the physiological context, large numbers of incapacitated macrophages mean inefficient immune response. Therefore, we also investigated whether the PH-Macrophages could regain their phagocytic ability. Upon measuring the intracellular ROS levels at different time points after phagocytosis with bacteria, we observed that the cytoplasmic ROS decrease with time over a period of 8 h (Fig. S5E). The cytoplasmic stiffness of cells exposed to 250 µM H_2O_2 for 1 h, measured 8 h post-H_2O_2 treatment, also shows a significant return of cytoplasmic stiffness to control conditions (Fig. S5F,G). This indicates that, after a span of ∼8 h, macrophages possibly regain their phagocytic ability. Cytoplasmic microrheology is a key regulator of multiple physiological processes, including cell morphology, proliferation, migration and differentiation. Our finding of ROS-mediated cytoplasmic stiffening may therefore modulate a myriad of physiological conditions as mentioned above. In addition, pathological conditions – such as cancer, diabetes, cardiomyopathy and a vast array of neurological disorders – have altered cytoplasmic rheology as well as erratic ROS production. Therefore, we believe that our findings are of wider and more general interest.

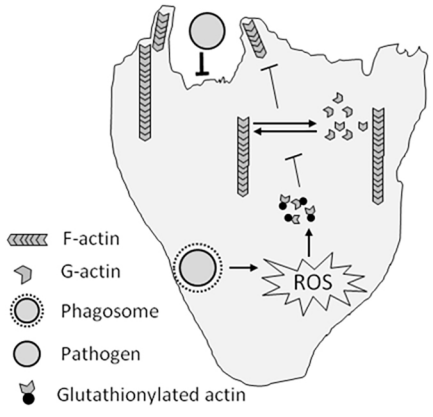

Fig. 6. ROS generated by the phagosome incapacitate the macrophage of its phagocytic ability. Schematic representation of the negative-feedback loop triggered in response to pathogen (bead or bacteria) engulfment. ROS oxidize actin, leading to glutathionylation of globular actin (G-actin), thus impairing intracellular actin turnover. This leads to stiffening of the cytoplasm and reduced ability of the macrophage for further phagocytosis.

MATERIALS AND METHODS

Cell culture

Experiments were performed on American Type Culture Collection-derived human monocytic leukaemia THP-1 cells and murine macrophage RAW264.7 cells. RPMI-1640 (Himedia) was used to culture THP-1 cells, while RAW 264.7 cells were cultured in Dulbecco's modified Eagle medium. Both culture media were supplemented with 10% heat-inactivated fetal bovine serum and 5% penicillin-streptavidin (Invitrogen and Himedia). RAW264.7 cells were transfected with mEGFP (pEGFP-N1, Addgene plasmid #6085-1) and actin–mEGFP (pCAG–mGFP–actin, plasmid #21948, Addgene) using Lipofectamine 3000 (Invitrogen) as per the prescribed protocol. Cells were treated for 30 min with 50 µM CK666 (Sigma-Aldrich), 2 µM Cytochalasin D (Sigma-Aldrich) and 10 µM phalloidin oleate (Sigma-Aldrich) (Rotty et al., 2017). The drugs mentioned above were dissolved in DMSO at appropriate concentrations. For FACS experiments, cells cultured on Petri dishes were incubated for the previously mentioned durations with saturating concentrations of beads or bacteria. Cells were then washed twice with 1× PBS and fixed with 4% paraformaldehyde at room temperature for 15 min. The fixed cells were washed with PBS and scraped from the cell culture plate for FACS analysis. For ROS analysis, cells were stained with 10 µM H_2DCFDA (Sigma-Aldrich) for 30 min in serum-free medium, and then microscope imaging or FACS experiments were performed. For Fig. S5E, PMA-treated cells were cultured in a 48-well plate at equal density for 24 h, incubated with saturating concentrations of bacteria for 1 h, rinsed thoroughly and then stained with H_2DCFDA at the indicated time points. Cells of a particular group were then lysed with 95% DMSO and the fluorescence of the lysate was measured in a spectrofluorometer.

Microscopy and image analysis

Time-lapse image acquisition for particle tracking was performed on a wide-field microscope (Zeiss Axio Observer Z1) using a high-speed complementary metal-oxide semiconductor (CMOS) camera (Hamamatsu Orca Flash 4.0). A confocal microscope (Zeiss LSM 880 Axio Observer) was used for fluorescence and DIC imaging. Images were acquired with a 63× (1.4 NA) oil immersion objective (Zeiss). Image analysis was performed with Fiji-ImageJ, MATLAB 2016a and Zen 2.0 (Zeiss).

Phagocytosis assay

Fluorescent carboxylated polystyrene beads of diameters 500 nm, 1 µm, 2 µm (F8888, Invitrogen) and 2.8 µm (M270 dynabeads, Thermo Fisher Scientific) were used as a bacterial mimetic for the phagocytosis assay. After incubation, cells were washed with 1× PBS to remove the excess beads. *Z*-stack imaging revealed the presence of beads inside cells. The maximum-intensity projection of the *Z*-stacks was obtained to calculate the percentage of phagocytic cells and the number of beads per cell. The same statistics were verified with FACS (BD Biosciences). For bacterial phagocytosis assay, the EGFP or the RFP-expressing *Escherichia coli* were streaked on a kanamycin-resistant agarose Petri dish. The next day, a single bacterial colony was picked up using a sterilized toothpick and suspended in 1× PBS. The concentration of bacteria was measured using an optical densitometry assay (absorbance at 650 nm). An appropriate amount (>10^5 bacteria/ml) of bacterial suspension was added to the RAW264.7 cells for phagocytosis assay.

Estimation of the propensity of engulfment (*p*) by macrophages

'p' was estimated using $p=n_c/(n_a+n_b+n_c)$, where n_a, n_b and n_c are the number of observed events of case A, case B and case C (see Fig. 3D), respectively.

Dual phagocytosis assay with beads or bacteria

Cells were first incubated with sufficient numbers of green fluorescent beads or bacteria for 30 min. After a thorough wash with PBS, the second phagocytosis assay was performed on the same cells with red fluorescent beads (of the same size) or the bacteria after a duration 't'. The percentage of phagocytic cells and the number of beads per cell were estimated from the fluorescence images independently of FACS.

Identification of macrophages with protrusion-retraction activity (aPR-Macrophage): s.d. image generation

A DIC image of a cell, taken on a wide-field microscope, is generated by utilizing the refractive index variation of the intracellular components. The visual contrast (pattern) arising from optical interference manifests as pixel intensity in a digital DIC image (Fig. S6A). In a DIC time-lapse video of a cell, the movement of the cytoplasmic bodies generates considerably large intensity variations in time (Fig. S6Aii) giving rise to higher s.d. (Fig. S6Bi,ii). The background region in the image exhibits the lowest temporal-intensity variation (Fig. S6Aii), giving rise to the lowest values of s.d. (Fig. S6Bi,ii), whereas the peripheral regions of the cell undergoing protrusion-retraction activity give rise to temporal-intensity variations (Fig. S6Aii) higher than the background but lower than the cell body (Fig. S6Bii). We utilize this segregation of s.d. values (Fig. S6Bii) to visualize the protrusion-retraction activity (Fig. S6Bi).

Temporal-intensity fluctuations at a given single pixel (x, y) can be quantified by calculating the s.d. of the intensity values in time:

$$stdev(x,y) = \frac{1}{T}\sqrt{I(x,y,t) - \overline{I(x,y,t)}},$$

where T is the total number of time-lapse images, $I(x, y, t)$ is the intensity of a single pixel at (x, y) at time t, and $\overline{I(x,y,t)}$ is the mean intensity of the pixel (x, y) averaged over time.

We further normalize the $stdev(x, y)$, as described below, to obtain $sd(x, y)$. This normalization is done so that same display scale (colour bar) can be applied to different DIC time-lapse images, irrespective of their mean grey levels. The mean grey levels of the images could change because of differences in exposure time, illumination levels, etc.

$$sd(x,y) = \frac{stdev(x,y) - \min[stdev]}{\overline{stdev(x,y)}},$$

where min[$stdev$] is the minimum value of the s.d. obtained from the set [$stdev(x, y)$]

A custom colour map (Fig. S6Bi) was implemented to denote the cell-edge fluctuations on the red side of the spectrum, while the internal cellular fluctuations were on the bluer side. The background fluctuations are marked black in this scheme. The custom macro is available on request.

Quantification of protrusion-retraction activity

Time-lapse DIC images of cells were acquired at a regular interval of 30 s for 1 h. Kymographs along the line perpendicular to the edge of the cells were computed from the time-lapse images to visualize the protrusion-retraction activity. From the kymograph, the trajectory of the cell edge (x, y, t) is estimated. The RMSD of the cell-edge trajectory is computed from $RMSD\ (\tau) = \sqrt{\langle [x(t) - x(t+\tau)]^2 + [y(t) - y(t+\tau)]^2 \rangle_t}$. To compare the protrusion-retraction activity of the aPR and iPR regions, we compared the RMSD (τ=30) values.

Particle-tracking microrheology

Carboxylated polystyrene fluorescence microspheres of diameter 200 nm (F8888-Invitrogen) were ballistically injected into the cells using a Helios gene gun delivery system (Bio-Rad), with 60–80 pound-force per square inch (PSI) pressure used for the RAW264.7 cells and 80–120 PSI used for the THP-1 cells. The gene gun was fired from a distance of 3–5 cm above the cells, followed by washing with 1× PBS to prevent any possibility of endocytosis or micropinocytosis.

Cells were then incubated at physiological conditions for 2–4 h before imaging. A total of 1000 images were captured for a region of interest at a frequency of 50 Hz. To obtain the trajectory, the spatial position of microsphere (intensity-weighted centroid) was assigned using the Mosaic plug-in of ImageJ. At least 5–10 beads per cell were tracked for computing the rheological parameters of the cytoplasm. From the trajectory the mean square displacement (MSD) of the particles, $MSD = \sqrt{\langle \Delta r^2(\tau) \rangle}$, was calculated using $\sqrt{\langle \Delta r^2\ (\tau) \rangle} = \langle [x(t+\tau) - x(t)]^2 + [y(t+\tau) - y(t)]^2 \rangle_t$ (where τ is the time lag and t is the elapsed time).

The viscoelastic moduli $G^*(\omega)$ of the cytoplasm as a function of frequency ω is calculated from MSD, as described elsewhere (Crocker and Hoffman, 2007; Lee et al., 2006; Hoffman and Crocker, 2009). Briefly,

$$G^*(\omega) = \left\{ \frac{2k_BT}{3\pi\alpha i\omega F_u\left[\sqrt{\langle \Delta r^2\ (\tau) \rangle}\right]} \right\},$$

where $F_u\left[\sqrt{\langle \Delta r^2\ (\tau) \rangle}\right]$ is the unilateral Fourier transform of the MSD, k_BT is the thermal energy of the tracer particle, α is the radius of the particle, $G^*(\omega)$ is the frequency-dependent complex shear modulus, which comprises the elastic $G'(\omega)$ and viscous modulus $G''(\omega)$ as $G^*(\omega)=G'(\omega)+iG''(\omega)$, where $G'(\omega) = |G^*(\omega)|\ cos\frac{\pi\alpha(\omega)}{2}$ and $G''(\omega) = |G^*(\omega)|\ sin\frac{\pi\alpha(\omega)}{2}$. MATLAB codes for computing $G^*(\omega)$ were kindly supplied by Maxine Jonas (Mason et al., 1997; Mason, 2000).

FRAP

FRAP was performed on RAW264.7 cells expressing actin–mEGFP using a confocal microscope at 63× magnification. A small circular area (of diameter 2 µm) in the aPR and iPR regions was selected for photobleaching. Fifty frames were acquired for normalization of the initial fluorescence signal, and then bleaching was performed by scanning the area with a 488-nm LASER beam operating at 100% power for 15 ms. Recovery was monitored for 60 s. From the acquired images, the mean intensity of the bleached region of interest was analysed for FRAP kinetics. The FRAP data were fitted to a single exponential recovery equation $I(t) = I_0\left(1 - e^{\frac{-t}{\tau_D}}\right)$ to extract the recovery time τ_D of actin–mEGFP.

Immunoprecipitation and western blotting

RAW264.7 cells were seeded in 100 mm tissue culture-grade Petri dishes and the phagocytosis assay was performed with fluorescent carboxylated beads (Invitrogen). Cells in a separate dish (not challenged with carboxylated beads) were used as a control. The phagocytic and non-phagocytic populations were sorted by FACS for western blotting, and each population of cells was lysed using a standard lysis protocol for western blotting. The lysate from each population was diluted 50 times in Bradford reagent and optical density (OD) was measured. Using the OD values, the lysate in each population was diluted accordingly to normalize the final protein concentration in each sample. Actin was pulled down using anti-β-actin monoclonal anti-mouse (A2228, Sigma-Aldrich)-bound protein A/G agarose beads (BioBharati Life Sciences) at 4°C overnight (3:100 dilution), then western blotting was performed with anti-GSH (1:1000 dilution), raised in rabbit (MBS2005791, MyBioSource) to assess actin glutathionylation. β-actin (raised in rabbit) was used as a loading control. CD68 (ab201340, Abcam, dilution 1:50) and CD35 (ab25, Abcam, dilution 1:200) immunostaining was performed as per a standard protocol.

Preparation of polyacrylamide gels

Polyacrylamide gels were prepared as described elsewhere (Elosegui-Artola et al., 2014; Tse and Engler, 2010). Briefly, glass coverslips were cleaned in 1:1 HCl-methanol solution and air dried. The dried coverslips were submerged in 0.1 N NaOH for 10 min, then rinsed with distilled water and again air dried. The glass coverslips were then activated with (3-aminopropyl)triethoxysilane (Sigma-Aldrich) for 5 min. They were then immersed in 1% glutaraldehyde solution for 30 min, rinsed with distilled water and air dried. A solution containing 0.5% ammonium persulphate, 0.05% tetramethylethylenediamine (Sigma-Aldrich) and 2 mg/ml NH-acrylate (Sigma-Aldrich) were mixed with different concentrations

of acrylamide and bis-acrylamide to generate gels of different rigidities. Then, 10 µl of this solution was placed on the centre of the activated coverslip and covered with 12 mm-diameter glass coverslips pre-treated with dichrolodimethylsilane (DCDMS). After gel polymerization, the coverslips were removed and the gels incubated with 100 µg/ml of either fibronectin (Sigma-Aldrich) or collagen I (Millipore) overnight at 4°C.

Acknowledgements
We acknowledge the institutional Central Scientific Services (CSS) facility for FACS and confocal microscopy, and Dr Dipyaman Ganguly, Indian Institute of Chemical Biology, Kolkata, for the PBMC culture facility.

Competing interests
The authors declare no competing or financial interests.

Author contributions
Conceptualization: M.A., D.K.S.; Methodology: M.A., P.B., A.B.; Software: M.A., P.B.; Validation: M.A., P.B., A.B.; Formal analysis: M.A., P.B., A.B.; Investigation: M.A., P.B., A.B.; Resources: D.K.S.; Data curation: M.A., P.B., A.B.; Writing - original draft: D.K.S.; Writing - review & editing: D.K.S.; Visualization: M.A., D.K.S.; Supervision: D.K.S.; Project administration: D.K.S.; Funding acquisition: D.K.S.

Funding
D.K.S. was supported by the Department of Science and Technology, Ministry of Science and Technology [SB/S0/BB-101/2013] and the Department of Biotechnology, Ministry of Science and Technology [BT/PR6995/BRB/10/1140/2012]. M.A. and A.B. were supported by a fellowship from Council of Scientific and Industrial Research. A.B. is additionally supported by a Shyama Prasad Mukherjee (SPM) fellowship. P.B. was supported by a fellowship from the Indian Association for the Cultivation of Science.

Supplementary information
Supplementary information available online at
http://jcs.biologists.org/lookup/doi/10.1242/jcs.236471.supplemental

References

Bhattacharya, A., Agarwal, M., Mukherjee, R., Sen, P. and Sinha, D. K. (2018). 3D micro-environment regulates NF-κβ dependent adhesion to induce monocyte differentiation. *Cell Death Dis.* **9**, 914. doi:10.1038/s41419-018-0993-z

Block, J., Schroeder, V., Pawelzyk, P., Willenbacher, N. and Köster, S. (2015). Physical properties of cytoplasmic intermediate filaments. *Biochim. Biophys. Acta Mol. Cell Res.* **1853**, 3053-3064. doi:10.1016/j.bbamcr.2015.05.009

Carneiro, V. M. A., Bezerra, A. C. B., Guimarães, M. D. C. M. and Muniz-Junqueira, M. I. (2012). Decreased phagocytic function in neutrophils and monocytes from peripheral blood in periodontal disease. *J. Appl. Oral Sci.* **20**, 503-509. doi:10.1590/S1678-77572012000500002

Chen, Y.-Q., Kuo, C.-Y., Wei, M.-T., Wu, K., Su, P.-T., Huang, C.-S. and Chiou, A. (2013). Intracellular viscoelasticity of HeLa cells during cell division studied by video particle-tracking microrheology. *J. Biomed. Opt.* **19**, 011008. doi:10.1117/1.JBO.19.1.011008

Crocker, J. C. and Hoffman, B. D. (2007). Multiple-particle tracking and two-point microrheology in cells. *Methods Cell Biol.* **83**, 141-178. doi:10.1016/S0091-679X(07)83007-X

Dupré-crochet, S., Erard, M. and Nüße, O. (2013). ROS production in phagocytes: why, when, and where? *J. Leukoc. Biol.* **94**, 657-670. doi:10.1189/jlb.1012544

Elosegui-Artola, A., Bazellières, E., Allen, M. D., Andreu, I., Oria, R., Sunyer, R., Gomm, J. J., Marshall, J. F., Jones, J. L., Trepat, X. et al. (2014). Rigidity sensing and adaptation through regulation of integrin types. *Nat. Mater.* **13**, 631-637. doi:10.1038/nmat3960

Flores, L. R., Keeling, M. C., Zhang, X., Sliogeryte, K. and Gavara, N. (2019). Lifeact-TagGFP2 alters F-actin organization, cellular morphology and biophysical behaviour. *Sci. Rep.* **9**, 9507. doi:10.1038/s41598-019-45276-y

Freeman, S. A. and Grinstein, S. (2014). Phagocytosis: receptors, signal integration, and the cytoskeleton. *Immunol. Rev.* **262**, 193-215. doi:10.1111/imr.12212

Gardel, M. L., Kasza, K. E., Brangwynne, C. P., Liu, J. and Weitz, D. A. (2008). Mechanical response of cytoskeletal networks. *Methods Cell Biol.* **89**, 487-519. doi:10.1016/S0091-679X(08)00619-5

Gordon, S. and Taylor, P. R. (2005). Monocyte and macrophage heterogeneity. *Nat. Rev. Immunol.* **5**, 953-964. doi:10.1038/nri1733

Grek, C. L., Zhang, J., Manevich, Y., Townsend, D. M. and Tew, K. D. (2013). Causes and consequences of cysteine S-glutathionylation. *J. Biol. Chem.* **288**, 26497-26504. doi:10.1074/jbc.R113.461368

Gupta, M., Sarangi, B. R., Deschamps, J., Nematbakhsh, Y., Callan-Jones, A., Margadant, F., Mège, R.-M., Lim, C. T., Voituriez, R. and Ladoux, B. (2015). Adaptive rheology and ordering of cell cytoskeleton govern matrix rigidity sensing. *Nat. Commun.* **6**, 7525. doi:10.1038/ncomms8525

Hale, C. M., Sun, S. X. and Wirtz, D. (2009). Resolving the role of actoymyosin contractility in cell microrheology. *PLoS ONE* **4**, e7054. doi:10.1371/journal.pone.0007054

Hameed, F. M., Rao, M. and Shivashankar, G. V. (2012). Dynamics of passive and active particles in the cell nucleus. *PLoS ONE* **7**, e45843. doi:10.1371/journal.pone.0045843

Han, S., Tie, X., Meng, L., Wang, Y. and Wu, A. (2013). PMA and ionomycin induce glioblastoma cell death: activation-induced cell-death-like phenomena occur in glioma cells. *PLoS ONE* **8**, e76717. doi:10.1371/journal.pone.0076717

Hoffman, B. D. and Crocker, J. C. (2009). Cell mechanics: dissecting the physical responses of cells to force. *Annu. Rev. Biomed. Eng.* **11**, 259-288. doi:10.1146/annurev.bioeng.10.061807.160511

Horn, L., Leips, J. and Starz-gaiano, M. (2014). Phagocytic ability declines with age in adult Drosophila hemocytes. *Aging Cell* **13**, 719-728. doi:10.1111/acel.12227

Jain, N., Moeller, J. and Vogel, V. (2019). Mechanobiology of macrophages: how physical factors coregulate macrophage plasticity and phagocytosis. *Annu. Rev. Biomed. Eng.* **21**, 267-297. doi:10.1146/annurev-bioeng-062117-121224

Kaplan, G. (1977). Differences in the mode of phagocytosis with Fc and C3 receptors in macrophages. *Scand. J. Immunol.* **6**, 797-807. doi:10.1111/j.1365-3083.1977.tb02153.x

Karavitis, J. and Kovacs, E. J. (2011). Macrophage phagocytosis: effects of environmental pollutants, alcohol, cigarette smoke, and other external factors. *J. Leukoc. Biol.* **90**, 1065-1078. doi:10.1189/jlb.0311114

Kosaka, C., Sasaguri, T., Ishida, A. and Ogata, J. (1996). Cell cycle arrest in the G2 phase induced by phorbol ester and diacylglycerol in vascular endothelial cells. *Am. Physiol. Soc.* **270**, C170-C178. doi:10.1152/ajpcell.1996.270.1.C170

Lavin, Y., Winter, D., Blecher-gonen, R., David, E., Keren-shaul, H., Merad, M., Jung, S. and Amit, I. (2014). Tissue-resident macrophage enhancer landscapes are shaped by the local microenvironment. *Cell* **159**, 1312-1326. doi:10.1016/j.cell.2014.11.018

Lee, J. S. H., Panorchan, P., Hale, C. M., Khatau, S. B., Kole, T. P., Tseng, Y. and Wirtz, D. (2006). Ballistic intracellular nanorheology reveals ROCK-hard cytoplasmic stiffening response to fluid flow. *J. Cell Sci.* **119**, 1760-1768. doi:10.1242/jcs.02899

Lee, H., Ferrer, J. M., Nakamura, F., Lang, M. J. and Kamm, R. D. (2010). Passive and active microrheology for cross-linked F-actin networks in vitro. *Acta Biomater.* **6**, 1207-1218. doi:10.1016/j.actbio.2009.10.044

Li, Z., Jiao, Y., Fan, E. K., Scott, M. J., Li, Y., Li, S., Billiar, T. R., Wilson, M. A., Shi, X. and Fan, J. (2017). Aging-impaired filamentous actin polymerization signaling reduces alveolar macrophage phagocytosis of bacteria. *J. Immunol.* **199**, 3176-3186. doi:10.4049/jimmunol.1700140

Liang, Z., Zhang, Q., Thomas, C. M. R., Chana, K. K., Gibeon, D., Barnes, P. J., Chung, K. F., Bhavsar, P. K. and Donnelly, L. E. (2014). Impaired macrophage phagocytosis of bacteria in severe asthma. *Respir. Res.* **15**, 72. doi:10.1186/1465-9921-15-72

Mason, T. G. (2000). Estimating the viscoelastic moduli of complex fluids using the generalized Stokes–Einstein equation. *Rheol. Acta* **39**, 371-378. doi:10.1007/s003970000094

Mason, T. G., Ganesan, K., van Zanten, J. H., Wirtz, D. and Kuo, S. C. (1997). Particle tracking microrheology of complex fluids. *Phys. Rev. Lett.* **79**, 3282-3285. doi:10.1103/PhysRevLett.79.3282

Mehta, A. J. and Guidot, D. M. (2017). Alcohol and the lung. *Alcohol Res.* **38**, 243-254.

Mofrad, M. R. K. (2009). Rheology of the cytoskeleton. *Annu. Rev. Fluid Mech.* **41**, 433-453. doi:10.1146/annurev.fluid.010908.165236

Oliva, J. L., Caino, M. C., Senderowicz, A. M. and Kazanietz, M. G. (2008). S-Phase-specific activation of PKC alpha induces senescence in non-small cell lung cancer cells. *J. Biol. Chem.* **283**, 5466-5476. doi:10.1074/jbc.M707576200

Papagiannopoulos, A., Sotiropoulos, K. and Pispas, S. (2016). Particle tracking microrheology of the power-law viscoelasticity of xanthan solutions. *Food Hydrocoll.* **61**, 201-210. doi:10.1016/j.foodhyd.2016.05.020

Ponti, A., Matov, A., Adams, M., Gupton, S., Waterman-Storer, C. M. and Danuser, G. (2005). Periodic patterns of actin turnover in Lamellipodia and Lamellae of migrating epithelial cells analyzed by quantitative fluorescent speckle microscopy. *Biophys. J.* **89**, 3456-3469. doi:10.1529/biophysj.104.058701

Rotty, J. D., Brighton, H. E., Craig, S. L., Asokan, S. B., Cheng, N., Ting, J. P. and Bear, J. E. (2017). Arp2/3 complex is required for macrophage integrin functions but is dispensable for FcR phagocytosis and in vivo motility. *Dev. Cell* **42**, 498-513.e6. doi:10.1016/j.devcel.2017.08.003

Sakai, J., Li, J., Subramanian, K. K., Mondal, S., Bajrami, B., Hattori, H., Jia, Y., Dickinson, B. C., Zhong, J., Ye, K. et al. (2013). Reactive oxygen species-induced actin glutathionylation controls actin dynamics in neutrophils. *Immunity* **37**, 1037-1049. doi:10.1016/j.immuni.2012.08.017

Segal, A. W. (2005). How neutrophils kill microbes. *Annu. Rev. Immunol.* **23**, 197-223. doi:10.1146/annurev.immunol.23.021704.115653

Stojkov, D., Amini, P., Oberson, K., Sokollik, C., Duppenthaler, A., Simon, H.-U. and Yousefi, S. (2017). ROS and glutathionylation balance cytoskeletal

dynamics in neutrophil extracellular trap formation. *J. Cell Biol.* **216**, 4073-4090. doi:10.1083/jcb.201611168

Taylor, P. R., Martinez-Pomares, L., Stacey, M., Lin, H.-H., Brown, G. D. and Gordon, S. (2005). Macrophage receptors and immune recognition. *Annu. Rev. Immunol.* **23**, 901-944. doi:10.1146/annurev.immunol.23.021704.115816

Theriot, J. A. and Mitchison, T. J. (1991). Actin microfilament dynamics in locomoting cells. *Nature* **352**, 126-131. doi:10.1038/352126a0

Tse, J. R. and Engler, A. J. (2010). Preparation of hydrogel substrates with tunable mechanical properties. *Curr. Protoc. Cell Biol.* **47**, 10.16.1-10.16.16. doi:10.1002/0471143030.cb1016s47

Tseng, Y., Kole, T. P. and Wirtz, D. (2002). Micromechanical mapping of live cells by multiple-particle-tracking microrheology. *Biophys. J.* **83**, 3162-3176. doi:10.1016/S0006-3495(02)75319-8

Van Citters, K. M. Van, Hoffman, B. D., Massiera, G. and Crocker, J. C. (2006). The role of F-Actin and myosin in epithelial cell rheology. *Biophys. J.* **91**, 3946-3956. doi:10.1529/biophysj.106.091264

Varol, C., Mildner, A. and Jung, S. (2015). Macrophages: development and tissue specialization. *Annu. Rev. Immunol.* **33**, 643-675. doi:10.1146/annurev-immunol-032414-112220

Wang, J., Boja, E. S., Tan, W., Tekle, E., Fales, H. M., English, S., Mieyal, J. J. and Chock, P. B. (2001). Reversible glutathionylation regulates actin polymerization in A431 cells. *J. Biol. Chem.* **276**, 47763-47766. doi:10.1074/jbc.c100415200

Winterbourn, C. C., Hampton, M. B., Livesey, J. H. and Kettle, A. J. (2006). Modeling the reactions of superoxide and myeloperoxidase in the neutrophil phagosome. *J. Biol. Chem.* **281**, 39860-39869. doi:10.1074/jbc.M605898200

Wirtz, D. (2009). Particle-tracking microrheology of living cells: principles and applications. *Annu. Rev. Biophys.* **38**, 301-326. doi:10.1146/annurev.biophys.050708.133724

Yeung, T., Georges, P. C., Flanagan, L. A., Marg, B., Ortiz, M., Funaki, M., Zahir, N., Ming, W., Weaver, V. and Janmey, P. A. (2005). Effects of substrate stiffness on cell morphology, cytoskeletal structure, and adhesion. *Cell Motil. Cytoskeleton* **60**, 24-34. doi:10.1002/cm.20041